J. Cent. South Univ. (2013) 20: 2275−2284
DOI: 10.1007/s11771-013-1734-1

Springer

Anisotropic characteristics of granular materials under simple shear

QIAN Jian-gu(钱建固)[1, 2], YOU Zi-pei(由子沛)[1, 2], HUANG Mao-song(黄茂松)[1, 2]

1. Key Laboratory of Geotechnical and Underground Engineering of Ministry of Education (Tongji University), Shanghai 200092, China;
2. Department of Geotechnical Engineering, Tongji University, Shanghai 200092, China

Abstract: The discrete element method was used to investigate the microscopic characteristics of granular materials under simple shear loading conditions. A series of simple tests on photo-elastic materials were used as a benchmark. With respect to the original experimental observations, average micro-variables such as the shear stress, shear strain and the volumetric dilatancy were extracted to illustrate the performance of the DEM simulation. The change of anisotropic density distributions of contact normals and contact forces was demonstrated during the course of simple shear. On the basis of microscopic characteristics, an analytical approach was further used to explore the macroscopic behaviors involving anisotropic shear strength and anisotropic stress-dilatancy. This results show that under simple shear loading, anisotropic shear strength arises primarily due to the difference between principal directions of the stress and the fabric. In addition, non-coaxiality, referring to the difference between principal directions of the strain rate and the stress, generates less stress-dilatancy. In particular, the anisotropic hardening and anisotropic stress-dilatancy will reduce to the isotropic hardening and the classical Taylor's stress-dilatancy under proportional loading.

Key words: simple shear; discrete element method; anisotropy; non-coaxiality

1 Introduction

Apart from proportional loading conditions such as biaxial or triaxial stress paths, the simple shear that involves the rotation of principal stress axis is a typical non-proporitonal loading. The simple shear condition is normally accepted as the same mode of deformation within a shear band. The simple shear is also predominant during earthquake shaking [1−3]. Numerous laboratory experiments [4−5] have been performed to explore the simple shear behaviors. These previous studies showed that due to the effects of principal stress rotation, the dilation and non-coaxiality under the simple shear significantly deviate from that under proportional loading. However, a complete understanding of the underlying mechanisms for simple shear condition is still lacking. Despite that simple shear deformation can be simulated in element tests, it is difficult to directly calibrate the rotation of principal stress axis in the simple shear devices (SSDs).

In order to achieve better understanding of the underlying mechanism of soil responses, discrete element method (DEM) has been resorted to simulate laboratory element tests [6−8]. DEM can provide details of the particle interactions that cannot be measured in the laboratory, leading to better understanding of micromechanical responses in granular materials. Nevertheless, existing DEM simulations are limited to the proportional loading conditions, under which the micro-mechanism associated with the rotation of principal stress direction is not included [9].

In this work, discrete particle simulations have been carried out to examine the detailed simple shear processes. In addition, by using homogenization techniques, micromechanical variables are upscaled to the macro model and then the effects of the rotation of principal stress direction have been demonstrated.

2 Numerical simulation

2.1 Simple shear test

The simple shear test can impose more uniform strains than the direct shear test mainly due to the better-defined side boundary conditions [5]. The most common type of SSD currently used is the Cambridge simple shear device (CAMSSD) as earlier reported by ROSCOE [4]. The simple shear boundaries have been

Foundation item: Projects(10972159, 41272291, 51238009) supported by the National Natural Science Foundation of China Project supported by the Fundamental Research Funds of the central Universities
Received date: 2012−09−10; **Accepted date:** 2013−04−10
Corresponding author: QIAN Jian-gu, Professor, PhD; Tel: +86−13661567152; E-mail: qianjiangu@tongji.edu.cn

illustrated in Fig. 1, in which the solid lines show the initial positions of the wall boundaries and the dashed lines represent the deformed positions. The two side walls rotate at a constant angular velocity about the toes of side walls. The top wall can move vertically with constant normal pressure while the bottom wall is always fixed.

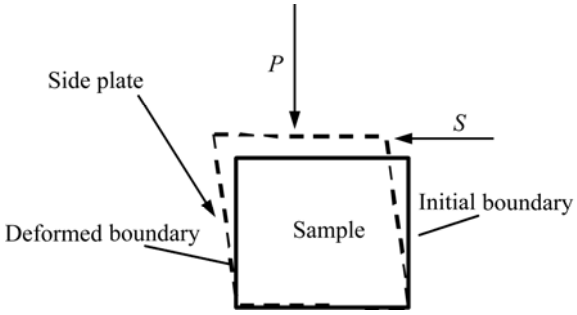

Fig. 1 Sketch of CAMSSD

ODA and KONISHI [10−11] conducted groups of simple shear tests of photoelastic material using CAMSSD. Photographs were taken during shear process to make statistics of contact normal. Right cylinders made by photoelastic material with the radii of 0.3, 0.4 and 0.5 cm and the length of 1.9 cm were arranged in random packing in a loading frame. The scale of the loading frame is 16 cm×16 cm. The mixing ratio of cylinders with these three different radii was 25:15:8 by the number. This mixture of cylinders was put into the plane polarized light and uniaxially loaded through a loading arm P up to 392 N (normal force, equal to about 130 kPa) in the rigid frame of two-dimensional simple shear apparatus with no lateral expansion. The initial void ratio is 0.22 for the dense packing model and 0.26 for the loose packing model. Two distinct boundary conditions during the simple shear test are shown in Fig. 2.

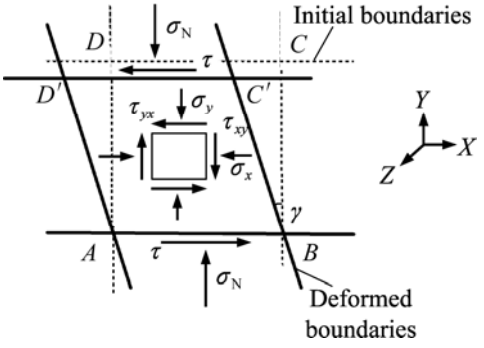

Fig. 2 Boundary conditions in simple shear test

As a type of non-proportional loading, the direction of the principal stress and principal strain rate will rotate during shearing process. The inclination angle can be obtained easily due to elastic mechanics.

$$\tan\theta_\sigma = \frac{2\tau_{xy}}{\sigma_y - \sigma_x} \tag{1}$$

$$\tan\theta_{\dot{\varepsilon}} = \frac{2\dot{\varepsilon}_{xy}}{\dot{\varepsilon}_y - \dot{\varepsilon}_x} \tag{2}$$

where θ_σ is the orientation of the principal stress, and $\theta_{\dot{\varepsilon}}$ is the orientation of the principal strain rate. Both of them refer to the same y-axis.

2.2 Procedure and parameters of simulation

In this work, numerical simulations were performed for this simple shear test using software PFC2D. The simulation mainly consists of the following steps:

(1) As shown in Fig. 3, four walls are created as rigid boundaries. The length of each wall is 24 cm, 50% longer than the height of specimen, so that large straining and rotation are allowed to take place during the shear deformation. Subsequently, 467 particles are generated to reach the initial dense state of specimen.

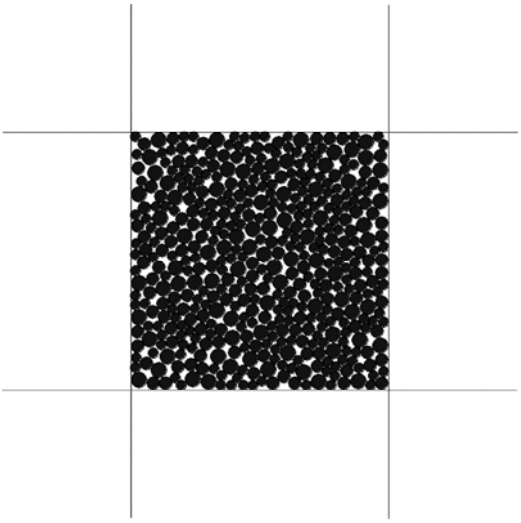

Fig. 3 Specimen in initial state

The interparticle contact law is viscoelastic, as stated by QIAN et al [12]. All material parameters for DEM simulations are listed in Table 1.

(2) At the first stage of consolidation, the normal stress 130 kPa is applied to the top surface of sample while other three rigid walls are used to form three other fixed boundaries.

(3) At the second stage of simple shear, two lateral walls will rotate about their toes with rotational velocity of 0.05 rad/s. In the meantime, the top wall is allowed to move horizontally with velocity of 8×10^{-3} m/s. During the second stage, consolidation pressure always keeps constant. It should be emphasized that for a laboratory simple shear test, only the stress and strain on the top boundary can be measured. It has been found that the top

Table 1 Material parameters for simulations of PFC

Parameter	Value
Total number of particles	467
Number of particles with the radii of 0.3, 0.4, 0.5 cm	243, 146, 78
Normal spring stiffness, k_n/Pa	1.0×10^8
Tangential spring stiffness, k_s/Pa	6.0×10^7
Local damping coefficients/(Pa·s)	0.7
Interparticle friction coefficient at consolidation state	1.0
Interparticle friction coefficient at shearing stage	0.4
Density of particles/(kg·m^{-3})	2 700
Friction coefficient between wall and particle	0.5

boundary stress in the sample is generally not uniform, and only the stress in the centre of sample can be seen as an ideally uniform state [13−14], as assumed within the macroscopic constitutive theory. With these considerations, we attempt to use the average data over the circle with radius of 60 mm in the center of sample instead of the top boundary, in DEM analysis.

3 Macro mechanic properties

Figure 4 presents the shear stress−strain behaviors and dilation responses for testing and DEM simulations, respectively.

It can be seen that DEM is able to reproduce the prepeak stress−strain and dilatancy responses for simple shear path, compared to the overall experimental observations on photoelastic materials. Nevertheless, it should be also noted that the present DEM tends to underestimate the shear stress level and overestimate the postpeak dilatation, with respect to experimental observations. This is primarily due to the following reasons: (1) the interparticle rolling resistance is not included in the present DEM simulation; (2) DEM data are obtained from the circle in the center of the sample while the experimental data are obtained on the top surface of the sample.

Figure 5 further shows the non-coaxiality, referring to the difference between the principle directions of stress and strain rate. In principle, the non-coaxiality should be attributed to material anisotropy, particularly for non-proportional loading [15]. Note that for proportional loading conditions, coaxiality is the basic assumption in framework of classical plasiticicty, based on the observations of proportional path tests such as biaxial or triaxial tests.

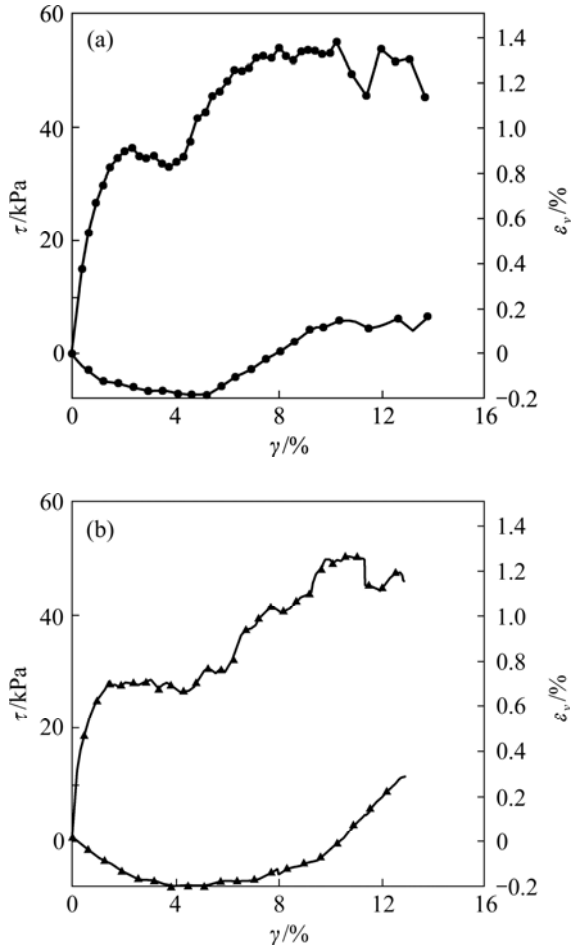

Fig. 4 Shear stress−shear strain and volumetric strain−shear strain responses for tests and DEM simulations: (a) Oda test data; (b) Simulation results

It can also be seen that this model provides a good approximation of non-coaxiality during simple shear loading. The simulation results are in good agreement with the original experimental data. And for the convenience in obtaining more data, the simulated curve is smoother than the original one.

Despite some quantitative difference between DEM simulations and the experimental observations, it is clear that the present DEM is able to reproduce the overall simple shear behaviors, specifically for the prepeak states that essentially correspond to the real constitutive responses [16].

4 Microscopic properties and anisotropies evolution

4.1 Evolution of contact normal

At the macro level, the mechanical behaviors of granular materials mainly depend on the interparticle contacts properties, namely the anisotropic distributions of contact normals and contact forces. For 2D problem,

the contact vector ($\boldsymbol{l}_i$), contact force ($\boldsymbol{f}_i$) and contact normal ($\boldsymbol{n}_i$) between two neighbor particles are presented in Fig. 6. Note that $\boldsymbol{l}_i$ denotes the vector that connects the centroids of two neighbor particles. l and $\boldsymbol{m}_i$ are the length and the unit vector of $\boldsymbol{l}_i$, respectively. $\boldsymbol{n}_i$ and $\boldsymbol{t}_i$ are the unit vector of normal vector and tangential vector, respectively.

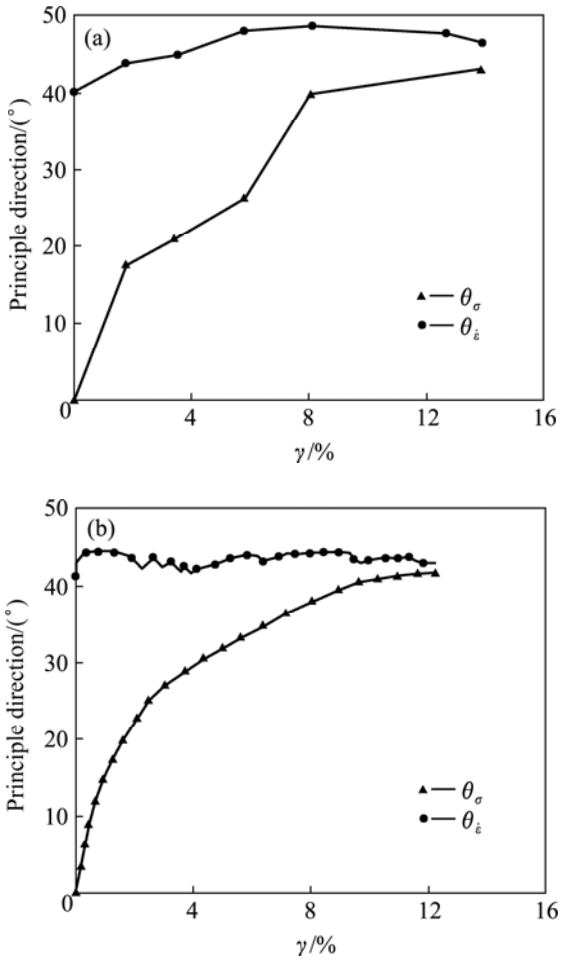

Fig. 5 Comparison of principle direction of stress and strain rate: (a) Test data; (b) DEM simulations

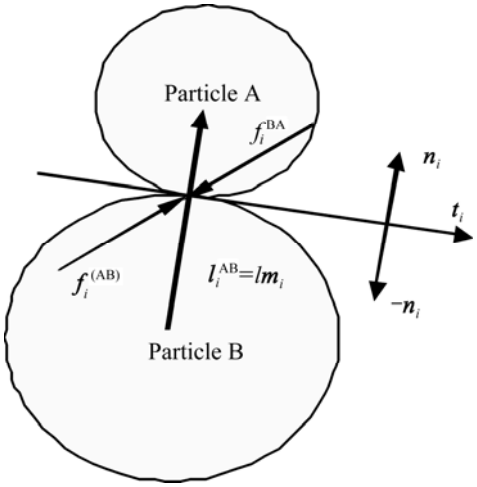

Fig. 6 Illustration of contact vector, contact force and contact normal

To investigate the micro-macro behaviors, attentions should be paid to the orientation distribution of contact normals, which is usually used to describe the feature of microstructure [17−18]. It should be emphasized that it is extremely difficult to measure the distribution of contact normals over all particles in our laboratory experiments, particularly for non-proportional loading conditions. In this work, the user-defined program using PFC2D code is intended to simulate the evolution of contact normals for the simple shear path.

According to ROTHENBURG and BATHURST [9], the preferred orientation of contact normals may be determined based on the frequency of contacts that fall within a certain angle interval. The overall frequency distributions of contact normals in various directions tend to be displayed as rose histogram (Fig. 7), essentially representing the fabric [19−22]. The orientation distribution of contact normal can be approximated by the second-order Fourier' function as

$$E(\theta)=\frac{1}{2\pi}\{1+a\cos 2(\theta-\theta_{\mathrm{a}})\} \tag{3}$$

where a is the anisotropic coefficient defining the degree of anisotropy, and θ_{a} is the direction angle of maximum distribution density of contact.

Analogous to anisotropic distribution of contact normals given by Eq. (3), the orientation distributions of contact normal force (f_{n}) and contact tangent force (f_{t}) may also be described as the following orientation-dependent functions [9]:

$$\bar{f}_{\mathrm{n}}=f_0\left[1+a_{\mathrm{n}}\cos 2\left(\theta-\theta_{\mathrm{n}}\right)\right] \tag{4}$$

$$\bar{f}_{\mathrm{t}}=-f_0\,a_{\mathrm{t}}\sin 2\left(\theta-\theta_{\mathrm{t}}\right) \tag{5}$$

where a_{n} and a_{t} represent the anisotropy degrees for the distribution of $\bar{f}_{\mathrm{n}}$ and $\bar{f}_{\mathrm{t}}$, respectively. The superposed bar denotes the average value within a certain angle interval (10° in this analysis). θ_{t} denotes their principal direction and $\bar{f}_0$ is the average value of f_{n} over all contacts.

Equation (3) may lead to the following equations:

$$\int_0^{2\pi}E(\theta)\sin 2\theta\mathrm{d}\theta=\frac{a}{2}\sin 2\theta_{\mathrm{a}} \tag{6a}$$

$$\int_0^{2\pi}E(\theta)\cos 2\theta\mathrm{d}\theta=\frac{a}{2}\cos 2\theta_{\mathrm{a}} \tag{6b}$$

Clearly, a and θ_{a} can be easily determined from Eq. (6). In the same way, Eqs. (4) and (5) may lead to

$$\int_0^{2\pi}E(\theta_{\mathrm{n}})\sin 2\theta\mathrm{d}\theta=\frac{a_{\mathrm{n}}}{2}\sin 2\theta_{\mathrm{n}} \tag{7a}$$

$$\int_0^{2\pi}E(\theta_{\mathrm{n}})\cos 2\theta\mathrm{d}\theta=\frac{a_{\mathrm{n}}}{2}\cos 2\theta_{\mathrm{n}} \tag{7b}$$

$$\int_0^{2\pi} E(\theta_t)\sin 2\theta \mathrm{d}\theta = \frac{a_t}{2}\cos 2\theta_t \tag{8a}$$

$$\int_0^{2\pi} E(\theta_t)\cos 2\theta \mathrm{d}\theta = \frac{a_t}{2}\sin 2\theta_t \tag{8b}$$

Analogously, a_n, θ_n, a_t and θ_t can be obtained from Eqs. (7) and (8).

Figure 7 shows the evolution of density distribution of contact normal with the development of shear strain. The solid lines represent the DEM simulations and the dashed lines represent the theoretical approximaiton using the second-order distribution density function given by Eq. (3).

It is shown that the frequency distribution of contact normals tends to concentrate on the Z axis at the initial shearing stage. As the shear strain increases, the degree of anisotropy (a) increases and the principal direction angle of the fabric rotates. During the shearing process, the redistribution of contact normals has a tendency that the density of contact normals increases near maximum compression and deceases near the minor compression. The principal direction of the fabric (i.e., direction with maximum density of contact normals) is always rotating towards the principal direction of stress (see Fig. 7). After the peak stress, the change of density distribution tends to reach a stable state. Meanwhile, the

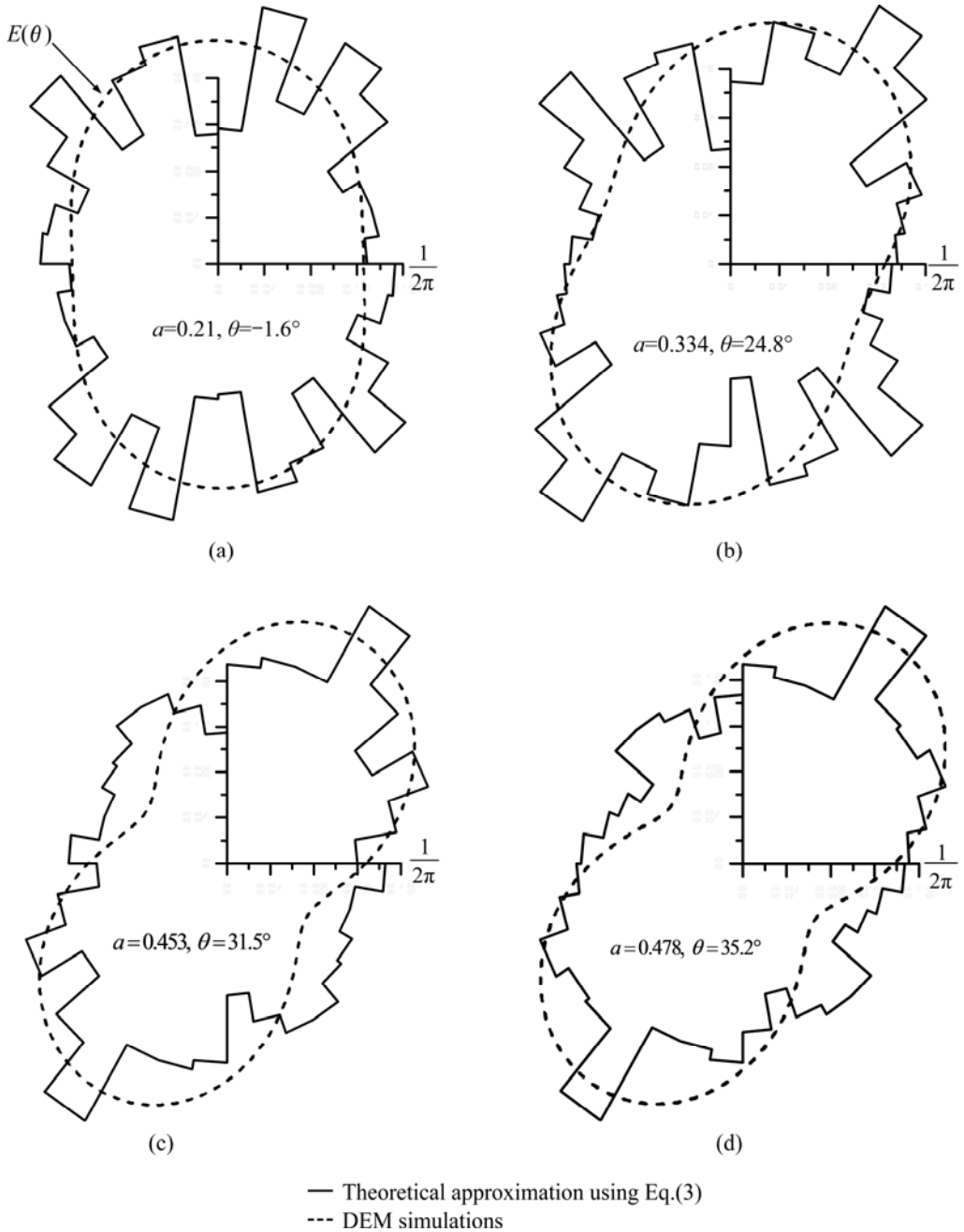

Fig. 7 Evolution of anisotropy of contact normals: (a) γ=0; (b) γ=0.04; (c) γ=0.09 (at peak stress state); (d) γ=0.13

degree of anisotropy has a fluctuant change and tends to reach a constant level. The evolution of fabric anisotropy is essentially in good agreement with previous study by QIAN et al [22].

4.2 Evolution of contact forces

4.2.1 Normal contact force

Figure 8 shows the evolution of anisotropies of contact normal force, namely orientation distribution of $\bar{f}_n / \bar{f}_0$. The solid lines and dashed lines represent the DEM simulations and the theoretical approximaiton given by Eq. (4), respectively. Departing from the density distribution of contact normals, anisotropy in the orientation distribution of contact normal force has a relatively low growing rate before the peak stress, particularly at the initial shearing. After the stress peak, the degree of anisotropy turns to have a decreasing rate. In addition, the preferred distribution orientation is rotating towards the principal direction of stress and almost keeping a fixed direction after the stress peak.

4.2.2 Tangential contact force

Figure 9 presents the anisotropic distribution of tangential contact forces. It is evident that the preferred orientation θ_t for the distribution of $\bar{f}_t$ is rotating with an increase of shear strain and in good agreement with θ_n. On the other hand, the value of a_t seems to be much small with respect to those of a and a_n, as illustrated in Fig. 10. Moreover, the theoretical

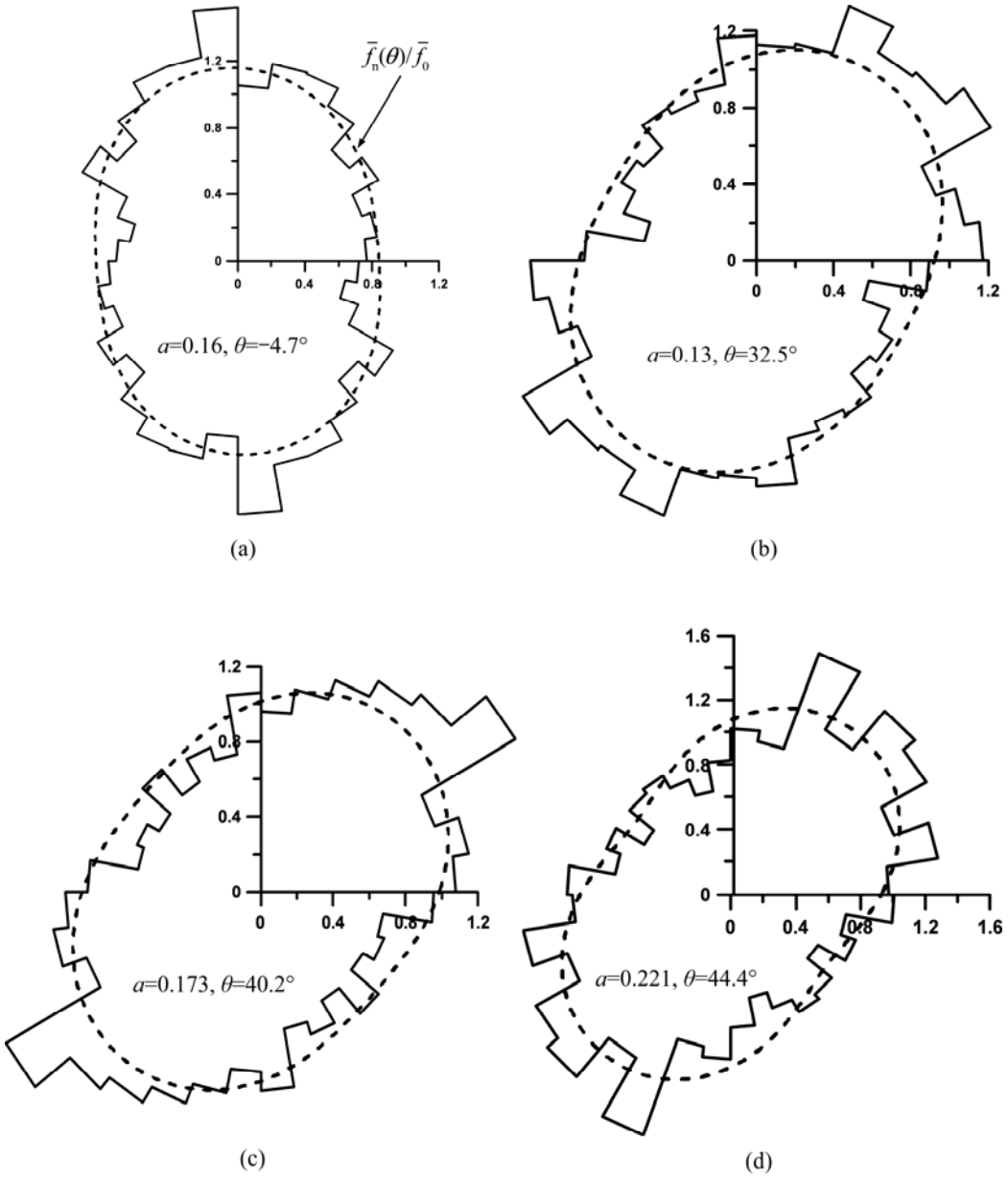

Fig. 8 Evolution of normal contact force: (a) γ=0; (b) γ=0.04; (c) γ=0.09 (peak stress state); (d) γ=0.13

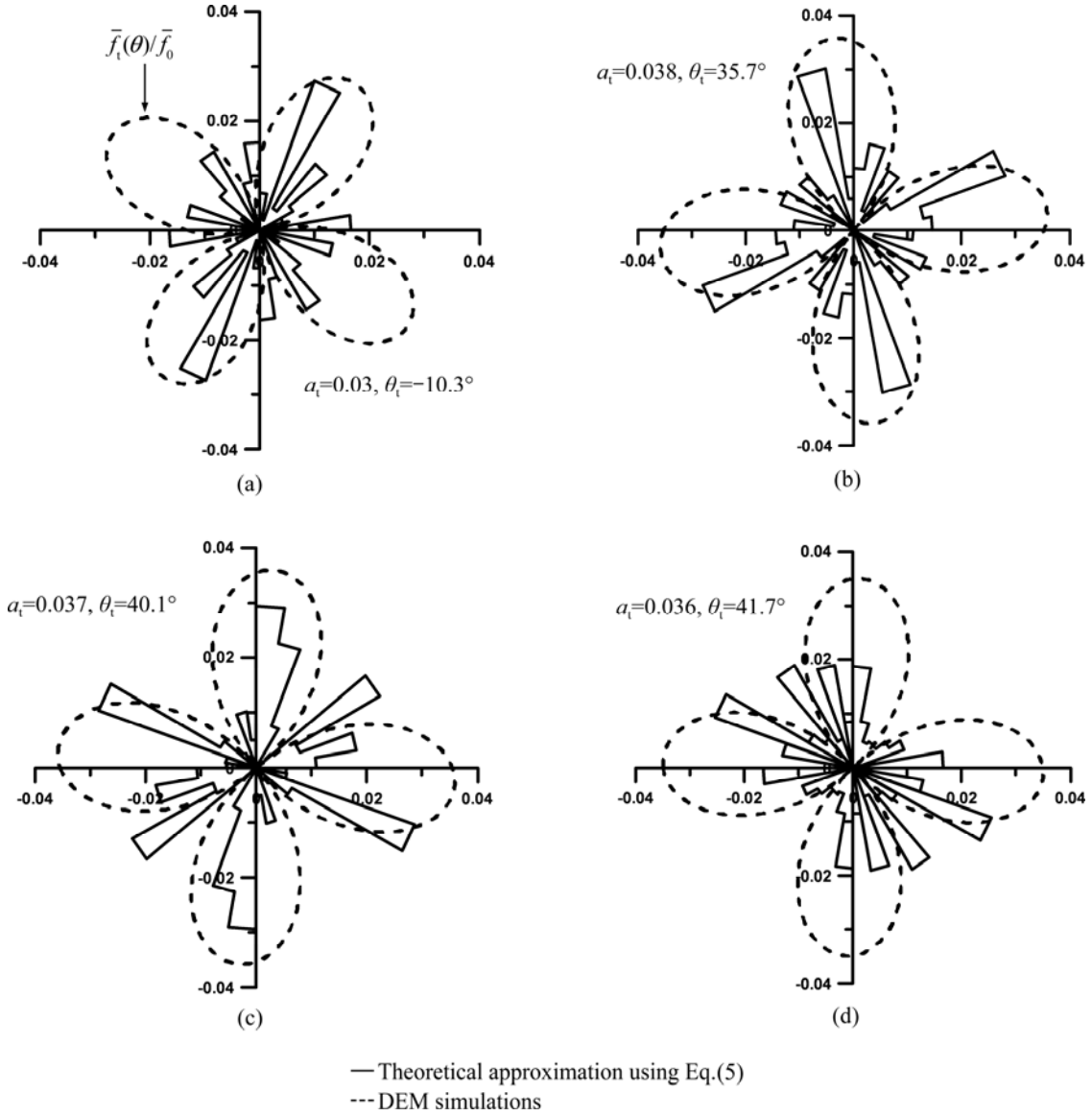

Fig. 9 Evolution of tangential contact force: (a) γ=0; (b) γ=0.04; (c) γ=0.09 (peak stress state); (d) γ=0.13

approximaiton of distribution of $\bar{f}_t$ by Eq. (5) does not fit the DEM simulations well after the stress peak. The deviation may be atrributed to the occurence of strain localization after the stress peak, at which the distribution becomes essentially non-uniform.

Figure 11 shows that the difference among the principal direction angles of contact normal vectors, contact normal force vectors and tangent contact force vectors. Clearly, the changes of θ_t, θ_n and θ_a have a consistent tendency to follow θ_σ during shear deformation. These principal directions tend to reach a saturation state when approaching the critical state. Moreover, the principal direction of stress always precedes that of contact normals but falls behind those of normal and tangential contact forces.

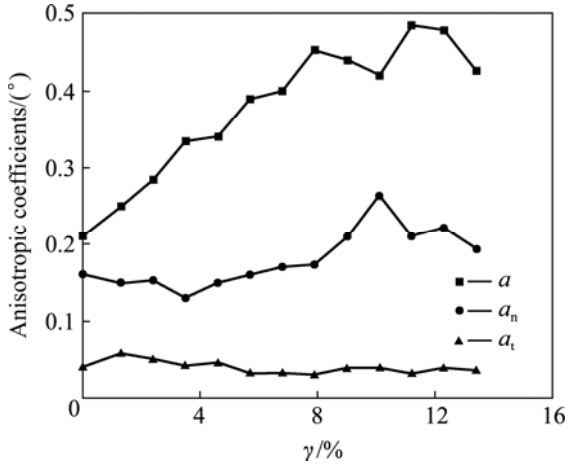

Fig. 10 Development of anisotropic coefficients a, a_n and a_t

4.3 Stress−fabric−force relationship

In this section, we attempt to upscale the above microscopic variables into the macroscopic variables for simple shear conditions.

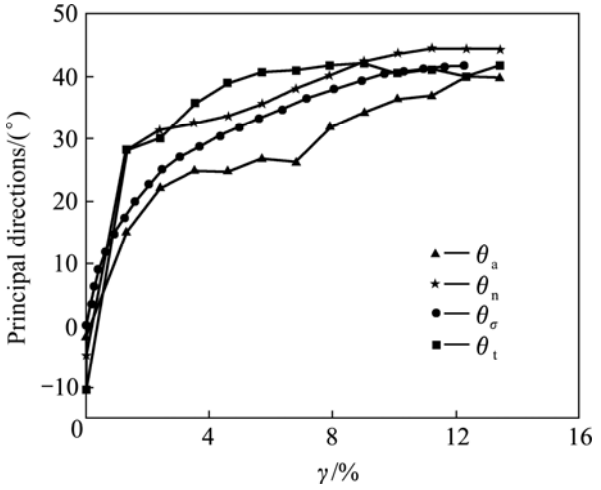

Fig. 11 Principal directions of contact normal, contact forces and stress

For simplicity, spherical particles are considered. In this case, $\boldsymbol{n}_i$ and $\boldsymbol{m}_i$ can be exchanged. Thus, the stress tensor in a unit volume can be associated with the interparticle contact forces as [9]

$$\boldsymbol{\sigma}_{ij}=\frac{1}{V}\sum^{N}l\left(f^{n}\boldsymbol{n}_i\boldsymbol{n}_j+f^{n}\boldsymbol{t}_i\boldsymbol{n}_j\right) \tag{9}$$

Note that anisotropy of the branch vector length is generally small for spherical particles. For this condition, the distribution of branch length is not correlated with the distribution of branch orientation, Equation (9) can be rewritten in the continuous form:

$$\boldsymbol{\sigma}_{ij}=2N\overline{l}\int_0^{\pi}E(\theta)\left(\overline{f}_n\,\boldsymbol{n}_i\boldsymbol{n}_j+\overline{f}_t\,\boldsymbol{t}_i\boldsymbol{n}_j\right)\mathrm{d}\theta \tag{10}$$

where N is the number of contacts over a unit volume; $\overline{l}$ is the average spacing of the centroids of two contact particles.

Substituting Eqs.(3)−(5) into Eq. (10), one finds the hydrostatic pressure:

$$p=\sigma_{ii}/2=N\overline{l}\int_0^{\pi}E(\theta)f^{n}\mathrm{d}\theta\approx\frac{1}{2}N\overline{l}f_0 \tag{11}$$

and the deviatoric stress components:

$$s_{11}=-s_{22}=\frac{p}{2}\left[a_{\mathrm{n}}\cos 2\theta_{\mathrm{n}}+a_{\mathrm{t}}\cos 2\theta_{\mathrm{t}}+a\cos 2\theta_0\right] \tag{12}$$

$$s_{12}=\frac{p}{2}\left[a_{\mathrm{n}}\sin 2\theta_{\mathrm{n}}+a_{\mathrm{t}}\sin 2\theta_{\mathrm{t}}+a\sin 2\theta_0\right] \tag{13}$$

where s_{ij} is the devietoric part of σ_{ij}. Equations (12) and (13) may lead to

$$\frac{q}{p}=\frac{1}{2}\left[a_{\mathrm{n}}\cos 2\left(\theta_{\mathrm{n}}-\theta_\sigma\right)+a_{\mathrm{t}}\cos 2\left(\theta_{\mathrm{t}}-\theta_\sigma\right)+a\cos 2\left(\theta_0-\theta_\sigma\right)\right] \tag{14}$$

where $q=\sqrt{s_{ij}s_{ij}/2}$ and θ_σ denotes the major principal direction of $\boldsymbol{\sigma}_{ij}$.

Equation (14) implies that the macroscopic shear strength depends on three factors: (1) a, representing the degree of fabric anisotropy; (2) a_{n} and a_{t}, representing the anisotropic degrees of contact forces; (3) difference between the principal directions of stress (θ_σ), contact normal vectors (θ_{a}) and contact force (θ_{t} and θ_{n}) vectors.

In Eq. (14), one should note that the mobilized friction angle (φ) can be related to the stress ratio by

$$\sin\varphi=\frac{q}{p}=\frac{\sigma_1-\sigma_3}{\sigma_1+\sigma_3} \tag{15}$$

It should be emphasized that for proportional loading $\theta_\sigma=\theta_{\mathrm{a}}=\theta_{\mathrm{n}}=\theta_{\mathrm{t}}$ as proposed by ROTHERNBURG and BATHURST [9]. Under this particular case, Eq. (14) will reduce to the following form:

$$\frac{q}{p}=\frac{1}{2}\left(a+a_{\mathrm{n}}+a_{\mathrm{t}}\right) \tag{16}$$

In order to validate the stress−fabric−force relationship, Fig. 12 shows the comparisons of computed results of q/p given by Eqs. (14−16), respectively. ROTHERNBURG and BATHURST [9] has earlier proposed that Eq. (16) can be used to estimate the overall shear strength under biaxial loading. However, Fig. 12 shows that Eq. (16) is not valid to represent the stress−fabric−force relationship due to ignorance of difference between θ_{a}, θ_{t}, θ_{n} and θ_σ. It indicates that the difference between principal directions of stress and these micro-variables (contact normal and contact force)

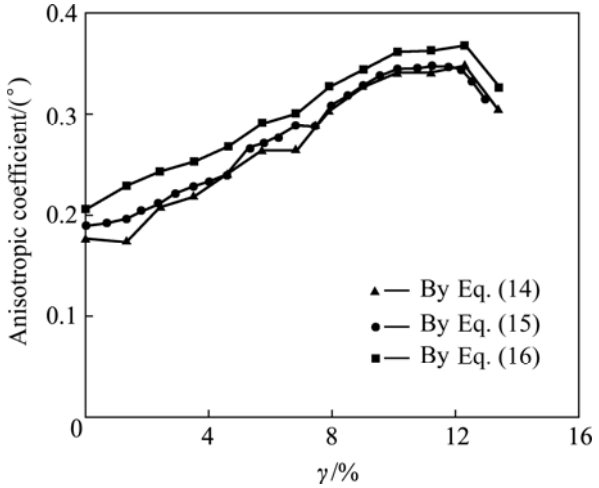

Fig. 12 Comparison of anisotropic coefficient and macroscopic parameters

in essence leads to a decreasing overall interparticle shear resistance.

4.4 Stress−dilatancy relationship

In two-dimensional plane−strain conditions, the dissipated energy is equal to the plastic work.

$$\dot{W} = \boldsymbol{\sigma}_{ij}\dot{\boldsymbol{\varepsilon}}_{ij} = (p\boldsymbol{\delta}_{ij} + \boldsymbol{s}_{ij})(\frac{\dot{\varepsilon}_v^p}{2}\boldsymbol{\delta}_{ij} + \dot{\boldsymbol{e}}_{ij}^p) = Mp\dot{\varepsilon}_s^p \tag{17}$$

where $\boldsymbol{\delta}_{ij}$ is Kronecker delta tensor; M is the stress ratio in critical state; $\boldsymbol{s}_{ij}$ and $\dot{\boldsymbol{e}}_{ij}^p$ are the components of deviatoric stress and deviatoric strain rate, which can be expressed as

$$\boldsymbol{s}_{ij} = q\begin{bmatrix} \cos 2\theta_\sigma & \sin 2\theta_\sigma \\ \sin 2\theta_\sigma & -\cos 2\theta_\sigma \end{bmatrix} \tag{18}$$

$$\dot{\boldsymbol{e}}_{ij}^p = \dot{\varepsilon}_s^p\begin{bmatrix} \cos 2\theta_{\dot{\varepsilon}} & \sin 2\theta_{\dot{\varepsilon}} \\ \sin 2\theta_{\dot{\varepsilon}} & -\cos 2\theta_{\dot{\varepsilon}} \end{bmatrix} \tag{19}$$

Substituting Eqs. (18) and (19) into Eq. (17) yields

$$p\dot{\varepsilon}_v^p + q\cos 2(\theta_\sigma - \theta_{\dot{\varepsilon}})\dot{\varepsilon}_s^p = Mp\dot{\varepsilon}_s^p \tag{20}$$

Equation (20) can be rewritten as

$$\frac{\mathrm{d}\varepsilon_v^p}{\mathrm{d}\varepsilon_s^p} = M - \frac{q}{p}\cos 2\left(\theta_\sigma - \theta_{\dot{\varepsilon}}\right) \tag{21}$$

Note that $\theta_\sigma - \theta_{\dot{\varepsilon}}$ essentially represents the degree of non-coaxiality between stress and strain rate tensors. As a result, Eq. (21) provides a non-coaxial version stress−dilatancy relationship. Clearly, $\theta_\sigma - \theta_{\dot{\varepsilon}}$, referring to coaxiality, holds for proportional loading such as biaxial compression. For this case, Eq. (21) is simplified to

$$\frac{\mathrm{d}\varepsilon_v^p}{\mathrm{d}\varepsilon_s^p} = M - \frac{q}{p} \tag{22}$$

which represents the classical Taylor's stress−dilatancy relationship.

With respect to DEM observations, Fig. 13 illustrates the difference between the proposed non-coaxial and coaxial (i.e., Taylor's) stress−dilatancy versions. Here, according to the sign convention in soil mechanics, compression is positive and dilation is negative.

It is clear that the coaxial stress−dilatancy theory always produces a liear relationship between the rate of dilation ($\mathrm{d}\varepsilon_v^p/\mathrm{d}\varepsilon_s^p$) and stress ratio (q/p). In comparison, the non-coaxial stress−dilatancy theory has created less dilatancy and non-linear relationship between stress ratio and dilation rate, in good agreement with DEM simulations.

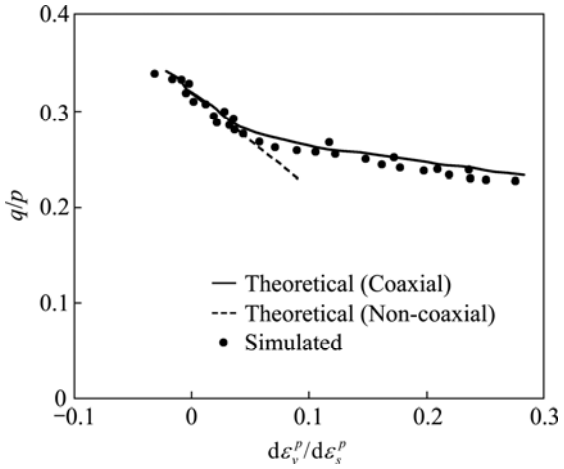

Fig. 13 Comparison of stress−dilatancy relationships

5 Conclusions

1) During the course of simple shear, the anisotropic degree in the density distribution of contact normals (representing the fabric) is significantly growing with the development of shear strain. The anisotropic degree in the density distribution of normal contact forces has a similar change trend but a lower magnitude with respect to the fabric anisotropy. On the other hand, the anisotropic degree in the density distribution of tangential contact forces is always keeping in a very low constant level.

2) During the shearing process, the principal directions (preferred distribution directions) of contact normal vectors, contact normal force vectors and tangent contact force have consistent developing tendency, namely following the principal direction of stress. Meanwhile, their principal directions tend to reach a saturation state at the critical state. In addition, the principal direction of stress always precedes that of contact normals but falls behind those of normal and tangent contact forces.

3) The non-coaxiality between the principal directions of the stress and micro-variables (contact normals, contact forces) produces significant effects on macro behaviors. In general, non-coaxiality will soften the overrall friction strength and cause less dilatancy. In addition, the non-coaxiality induces non-linear stress−dilatancy relationship, departing from the classical linear Taylor's stress-dilatancy.

References

[1] THORNTON C, ZHANG L. A numerical examination of shear banding and simple shear non-coaxial flow rules [J]. Philosophical Magazine, 2006, 86(21/22): 3425−3452.

[2] MARTE GUTIERREZ, WANG J, YOSHIMINE M. Modeling of the simple shear deformation of sand: Effects of principal stress rotation

[J]. Acta Geotechnica, 2009, 4(3): 193−201.

[3] SEGAL V M. Materials processing by simple shear [J]. Materials Science and Engineering, 1995, 197(2): 157−164.

[4] ROSCOE K H. The influence of strains in soil mechanics [J]. Géotechnique, 1970, 20(2): 129−170.

[5] COLE E R L. The behaviour of soils in the simple shear apparatus [D]. Cambridge: University of Cambridge, 1967.

[6] CUNDALL P A, STRACK O D L. The distinct element method as a tool for research in granular media. Part I [R]. Minneapolis: Tech Rept Dept Civil and Mineral Engrg, University of Minnesota, 1979.

[7] CUNDALL P A, STRACK O D L. A discrete numerical model for granular assemblies [J]. Geotechnique, 1979, 29(1): 47−65.

[8] CUNDALL P A, STRACK O D L. Numerical experiments on localization in frictional materials [J]. Ingenieur-Archiv, 1989, 59(2): 148−159.

[9] ROTHENBURG L, BATHURST R J. Analytical study of induced anisotropy in idealized granular materials [J]. Geotechnique, 1989, 39(4): 601−614.

[10] ODA M, KONISHI J. Rotation of principal stresses in granular material during simple shear [J]. Soils and Foundations, 1974, 14(4): 39−53.

[11] ODA M, KONISHI J. Microscopic deformation mechanism of granular material in simple shear [J]. Soils and Foundations, 1974, 14(4): 25−38.

[12] QIAN J G, HUANG M S, SUN H Z. Macro-micromechanical approaches for non-coaxiality of coarse grained soils [J]. Science China: Technological Sciences, 2011, 54(s1): 147−153. (in Chinese)

[13] DUNCAN J M, DUNLOP P. Behaviorofsoils in simple shear tests[C]//Proceedings of the 7th International Conference on Soil Mechanics and Foundation. Mexico, 1969: 101−109.

[14] DOUNIAS G T, POTTS D M. Numerical analysis of drained direct and simple shear tests [J]. Journal of Geotechnical Engineering, 1993, 119(12): 1870−1891.

[15] HILL R. The mathematical theory of plasticity [M]. Oxford, UK: The Clarendon Press, 1950.

[16] QIAN J G, YANG J, HUANG M S. Three-dimensional non-coaxial plasticity modeling of shear band formation in geomaterials [J]. Journal of Engineering Mechanics, ASCE, 2008; 34(4): 322−29. (in Chinese)

[17] ODA M. The mechanism of fabric changes during compressional deformation of sand [J]. Soils and Foundations, 1972, 12(2): 1−18.

[18] MURAYAMA S, MATSUOKA H. A microscopic consideration on the shearing behavior of granular materials using two dimensional model [A]// Disaster Prevention Research Institute Kyoto University, 1970, 13B: 1−19.

[19] ODA M. Micro-fabric and couple stress in shear bands of granular materials [J]. Powders and Grains, 1993, 3: 161−167.

[20] OUADFEL H A, ROTHENBURG L. Stress-force-fabric relationship for assemblies of ellipsoids [J]. Mechanics of Materials, 2001, 33(4): 201−221.

[21] YANG Z X, Li X S, YANG J. Quantifying and modelling fabric anisotropy of granular soils [J]. Geotechnique, 2008, 58(4): 237−248.

[22] QIAN Jian-gu, YOU Zi-pei, HUANG Mao-song, GU Xiao-qiang. A micromechanics-based model for estimating localized failure with effects of fabric anisotropy [J]. Computers and Geotechnics, 2013, 50: 90−100.

(Edited by HE Yun-bin)